

***p*-type to *n*-type conductivity transition in thermoelectric CoSbS**

Cite as: APL Mater. 10, 091104 (2022); <https://doi.org/10.1063/5.0107277>

Submitted: 04 July 2022 • Accepted: 16 August 2022 • Published Online: 13 September 2022

H. Sajida Kousar, Divya Srivastava, Antti J. Karttunen, et al.

COLLECTIONS



[View Online](#)



[Export Citation](#)



CrossMark

p-type to n-type conductivity transition in thermoelectric CoSbS

Cite as: APL Mater. 10, 091104 (2022); doi: 10.1063/5.0107277

Submitted: 4 July 2022 • Accepted: 16 August 2022 •

Published Online: 13 September 2022



View Online



Export Citation



CrossMark

H. Sajida Kousar, Divya Srivastava, Antti J. Karttunen, Maarit Karppinen,^{a)} and Girish C. Tewari^{a)}

AFFILIATIONS

Department of Chemistry and Materials Science, Aalto University, FI-00076 Aalto, Finland

^{a)}Authors to whom correspondence should be addressed: maarit.karppinen@aalto.fi and girish.tewari@aalto.fi

ABSTRACT

We demonstrate a *p*-type to *n*-type conductivity transition for thermoelectric CoSbS achieved by precisely controlling the sulfur vapor pressure during the sample synthesis. The *p*–*n* transition is experimentally confirmed by both the Seebeck coefficient and the Hall effect measurements. From the crystal structure refinements, the increase in the sulfur vapor pressure in the synthesis is weakly but steadily reflected in the occupancy factor of sulfur in the CoSbS lattice, while the *p*–*n* transition is seen as a peak in all the three lattice parameters, *a*, *b*, and *c*. Computationally, the situation could be simulated with first principle DFT calculations on compressed CoSbS. Without compression, DFT presents CoSbS as a *p*-type semiconductor with an indirect bandgap of 0.38 eV, while the pressure application results in an *n*-type semiconductor with decreased lattice parameters but the same indirect bandgap as in the uncompressed case. Experimentally, the thermal conductivity is strongly enhanced for sulfur-deficient samples, which could be due to larger phonon mean free paths. The sulfur loading significantly enhances the electrical conductivity while moderately decreasing the Seebeck coefficient such that the overall power factor is improved by a factor of 9 for the *n*-type sample and by a factor of 6 for the *p*-type sample, owing to the increased charge carrier density, although the performance is still relatively low. Thus, this study highlights CoSbS as a promising building block for thermoelectric devices based on its bipolar semiconductor nature with the possibility for both *p*-type and *n*-type doping with enhanced power factor.

© 2022 Author(s). All article content, except where otherwise noted, is licensed under a Creative Commons Attribution (CC BY) license (<http://creativecommons.org/licenses/by/4.0/>). <https://doi.org/10.1063/5.0107277>

I. INTRODUCTION

Semiconductors are the cornerstone materials of numerous modern applications, such as electronics, photonics, and energy harvesting and conversion [photovoltaic and thermoelectric (TE)] technologies.^{1–16} Apart from the elemental semiconductors, namely, silicon and germanium, many binary and ternary compound semiconductors are also employed, such as ZnSnN,¹ AlN,² InN,² ZnS,³ Mg₃Sb₂,^{4,5} AlGaN,^{9–11} HgIn₂Te₄,¹² GaN,^{2,13,14} and GaAs.^{15,16} One of the benefits of binary and ternary semiconductors is the possibility to control physical properties through intrinsic compositional tuning. Most excitingly, in a few cases, such tuning can even switch the type of the charge carriers, i.e., result in *n*-type to *p*-type transition, or vice versa. An important example is the Zintl compound, Mg₃Sb₂, which may exhibit either *n*-type (with Mg excess) or *p*-type (Sb excess) conductivity depending on the Mg vs Sb composition.^{4,5} Another interesting system is the Cr_{2+x}Se₃, which also shows a *p*-type to *n*-type conductivity transition with an increase in the Cr content.¹⁷ These are particularly promising considering the

application of such materials in thermoelectric (TE) devices, which requires mutually compatible *n*-type and *p*-type materials.

For both the *n*-type and *p*-type TE materials, the heat-to-electricity conversion efficiency is assessed based on the dimensionless figure-of-merit, $ZT = \frac{\sigma S^2 T}{\kappa}$, in which S is the absolute value of the Seebeck coefficient; the sign of S is negative/positive for *n*-type/*p*-type material. Hence, the high ZT value can be achieved in a material with high values for S and electrical conductivity (σ) together with a low value for thermal conductivity (κ).^{18,19}

Among the various TE material candidates,^{20–25} the metal sulfides have attracted considerable interest as potential tellurium-free alternatives,²⁶ and one of those is Paracostibite (CoSbS), which is now rapidly gaining attention owing to its promising TE performance and flexibility for chemical substitutions at each of its three atomic sites.^{27–29} In its orthorhombic (space group *Pbca*) unit cell consisting of eight Co(Sb,S)₃ octahedra, each Co atom is coordinated to three Sb and three S atoms.^{30–32} Previous works have already demonstrated substantially enhanced power factor ($PF = \sigma S^2$)

values and lowered thermal conductivity values for CoSbS realized through different doping, alloying, nanostructuring, or ball milling schemes. However, the type of conductivity, i.e., *n*-type or *p*-type, has remained somewhat controversial.

In most of the early studies, CoSbS has been reported as an *n*-type semiconductor with a negative Seebeck coefficient value and rather heavy conduction and valence bands (VB) in the typically measured 200–800 K temperature range. The most commonly applied chemical substitutions in CoSbS, such as Ni on the Co site, Te on the Sb site, or Se on the S site, were typically found to increase the electron density and enhance the *n*-type conduction in the whole temperature range.^{33–38} However, in our recent work, we found positive Seebeck coefficient values for CoSbS below room temperature,³⁹ which was later confirmed in other studies.⁴⁰ Most interestingly, for some CoSbS samples, a crossover from *n*-type to *p*-type conduction was observed below 500 K upon cooling,^{41–44} and similarly for Cu-for-Co and Se-for-S substituted samples below 475 K.^{41,44} These findings imply the possibility of the bipolar nature of CoSbS. However, no systematic efforts have been reported to truly verify this possibility and understand it more deeply.

Here, we demonstrate that through systematic control of the precise sulfur content in CoSbS, it is possible to systematically tailor its conduction type, from *p*-type to *n*-type. We utilize this simple compositional tuning to maximize the power factor for both the *n*-type and *p*-type CoSbS material variants. Moreover, since the sulfur-content variation is reflected in the lattice parameters, we show that, computationally, the situation can be simulated with first principles density functional theory (DFT) calculations through a compressive pressure application.

II. EXPERIMENTAL DETAILS

A series of polycrystalline CoSb_{1+x} samples with the nominal sulfur content x varying from +0.10 to -0.10 were synthesized through solid-state synthesis from appropriate quantities of elemental precursors, i.e., Co powder (99.8%), Sb shots (99.99%), and S shots (99.99%), by adding 0, 5, or 10% extra/less sulfur in the precursor mixture. The precursors were carefully mixed inside a glove box, pelletized, and sealed in quartz ampoules under vacuum for heat treatment in a tube furnace. In the case of the sulfur excess, the added extra sulfur created a homogeneous vapor pressure in the sealed tube at a high temperature. The first heat treatment was carried out at 800 °C for 24–48 h inside a tube furnace, followed by natural cooling to room temperature. The tube furnace creates a natural temperature gradient, and at the end of the heat treatment, the excess sulfur is collected at the colder end of the sealed tube. The resultant charge was ground and thoroughly homogenized by using an agate mortar and pestle in an argon-filled glovebox, and then, the powders were again pressed into pellets and sealed in quartz ampoules under vacuum for the second heat treatment at 750 °C for 24 h followed by natural cooling.

Each sample was characterized for the phase purity and crystal structure determination by x-ray diffraction (XRD; PANalytical X'Pert PRO MPD Alpha-1; Cu K α 1 radiation). The low temperature transport properties were measured by using a physical property measurement system (PPMS; Quantum Design; equipped with 9 T magnet). The electrical resistivity (ρ), the Seebeck coefficient (S),

and the thermal conductivity (κ) were measured simultaneously by using the thermal transport option (TTO) available in the PPMS. The Hall measurements were carried out by using a standard four-point-probe technique. In the TTO measurement, we make four linear probe connections to a rectangular shape (roughly 10 × 4 × 1 mm³) sample along its length. A heater is attached to one end probe and two thermometers are attached to the middle probes. In isothermal condition, the heater applies heat to one end of the sample, and the temperature difference and the Seebeck voltage are measured simultaneously from the middle probes at the steady state. The Seebeck voltage is divided by the temperature difference to obtain the Seebeck coefficient. The thermal conductivity was estimated by using sample dimensions and the temperature difference.

Density functional theory calculations were carried out in a generalized gradient approximation (GGA) framework as implemented in QUANTUM ESPRESSO.^{45,46} The Perdew–Burke–Ernzerhof (PBE) exchange correlation function⁴⁷ was used with scalar relativistic ultrasoft pseudopotentials from GBRV (<http://www.physics.rutgers.edu/gbrv/>) high-throughput pseudopotentials library.⁴⁸ The spin–orbit coupling (SOC) was not included in the calculations. The plane wave basis cut-off was taken to be 70 Ry.

The reducible Brillouin zone was sampled by using the Monkhorst–Pack type k-point mesh of 11 × 11 × 11 for self-consistent calculations. The lattice parameters for uncompressed and compressed CoSbS lattices were obtained by performing the structural optimization, where both the atomic positions and lattice parameters were free to vary. For the compressed system, the target pressures were fixed to 10 and 20 kbar during the optimization. All the electronic structure calculations were performed with the optimized lattice parameters. The Seebeck coefficient was calculated in a temperature range of 5–300 K by using the Boltzmann transport equations and constant relaxation time approach as implemented in BoltzTraP2.⁴⁹

III. RESULTS AND DISCUSSION

A. Structural analysis

All the CoSb_{1+x} ($x = 0.10, 0.05, 0.0, -0.05, -0.10$) samples were found to be phase-pure of the orthorhombic Paracostibite structure with space group Pbca;^{28,29,31} the XRD patterns are presented in supplementary material (Fig. S1). Even for the highest sulfur excess used in the synthesis, i.e., $x = 0.10$, no trace of leftover elemental sulfur was seen in the samples, within the detection limit of XRD. The examination of the XRD data in detail indicated that the orthorhombic symmetry with space group Pbca is preserved throughout the sample series. The Rietveld refinement results presented in Table S1 show that the occupancy factor of the S-site slightly but monotonously increases with x . However, the lattice parameters behave differently; that is, with increasing nominal sulfur content x , the lattice parameters first increase up to $x \approx 0$ and then decrease for $x > 0$, as shown in Fig. 1(a). Computationally, we simulated the lattice contraction in stoichiometric CoSbS through a compressive pressure application. From Fig. 1(b), the DFT optimized lattice parameters show a similar systematic decrease with pressure as experimentally seen by increasing or decreasing the sulfur in the sample synthesis beyond $x \approx 0$. Most interestingly, we will show later in this paper that the turning point at $x \approx 0$ corresponding

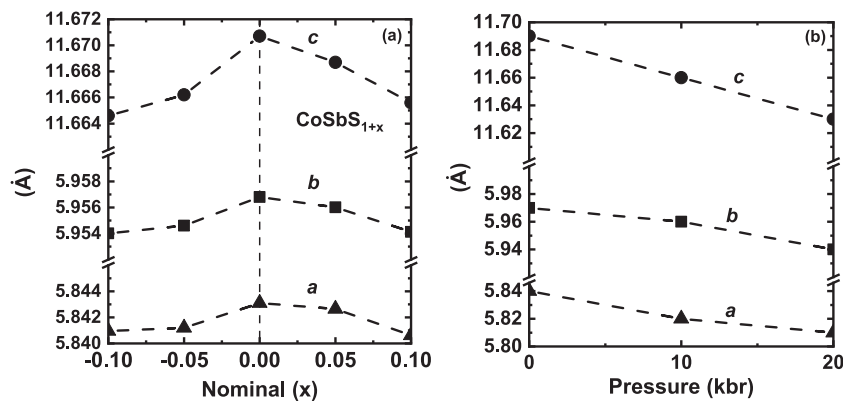


FIG. 1. (a) XRD-refined lattice parameters plotted against nominal sulfur content x (used in synthesis) for the CoSbS_{1+x} samples. (b) DFT-optimized lattice parameters of CoSbS with increasing pressure.

to the largest unit cell volume also marks the point where the *p*-type electrical conductivity turns into the *n*-type conduction.

B. Band structure

The DFT optimized lattice parameters mimicked the experimentally seen sulfur-excess trend, and the absolute values were also in very good agreement (within 0.2%) with the experimental lattice parameters for the $x = 0.0$ sample. The stoichiometric CoSbS appears as a *p*-type semiconductor both experimentally and computationally; however, with increasing sulfur excess used in the synthesis and contracting lattice parameters, a distinct polarity reversal from *p*-type to *n*-type conduction is observed. To understand this polarity reversal, we exploited the DFT calculations on compressed CoSbS by applying hydrostatic pressure of 10 or 20 kbar. The comparison between the experimental and DFT-optimized lattice parameters, as shown in Fig. 1, indicates that the computational lattice contraction is significantly larger in magnitude than that of the experimental lattice contraction.

Next, we plot in Fig. 2 the calculated band structures for uncompressed and compressed (10 and 20 kbar) CoSbS . While in the uncompressed CoSbS , the Fermi level is closer to the valence bands, the Fermi level of the compressed CoSbS shifts closer to the conduction bands (CB). The band structures of uncompressed and compressed CoSbS phases are very similar in the sense that they show a multi-valley behavior. The indirect bandgap of uncompressed CoSbS is 0.38 eV, and this does not change when compression is applied. However, compression increases the Fermi level, and the Fermi level moves up closer to the conduction band, implying *n*-type behavior. If the Fermi level of uncompressed CoSbS is considered as a reference Fermi level, the Fermi level shifts by 0.25 eV for 10 kbar and by 0.43 eV for 20 kbar compressions up toward the conduction band (CB). Near the Fermi level, the electronic states in CB and valence band (VB) are mainly dominated by the Co-3d orbitals, with small Sb-5p and S-3p orbital contributions, whereas Co-3p, Sb-5s, and S-3s orbitals contribute very little, see Fig. 2. Compression does not significantly change the orbital component contribution near the Fermi level; however, it adds few states into the CB.

In CoSbS , the Co atoms are octahedrally coordinated to three Sb atoms and three S atoms. In the case of uncompressed CoSbS , the three S atoms are at distances of 2.29, 2.31, and 2.28 Å, and

the three Sb atoms are at distances of 2.57, 2.54, and 2.53 Å, while the distance between Sb and S atoms is 2.55 Å. The Bader atomic charges are 16.84 e^- for Co, 14.51 e^- for Sb, and 6.65 e^- for S, indicating a transfer of 0.16 e^- from Co and 0.49 e^- from Sb to S, which thus has gained 0.65 e^- . This suggests relatively covalent or polarized covalent chemical bonds. On pressure application, the distances between the Co and S/Sb atoms decreased slightly differently, and the Co to S/Sb distance shortened by 0.4%/0.3% upon 10 kbar and 1.0%/0.6% upon 20 kbar. The Bader atomic charge analysis on the compressed systems indicates no significant change in charges on Co, Sb, and S atoms. However, the Co-Sb and Co-S bonds get shorter on compression.

C. Charge carrier density

The Hall-effect measurements were employed to determine the charge carrier type and density in our CoSbS_{1+x} samples, see Fig. 3. The Hall resistance (R_{XY}) vs the magnetic field (B) data measured at different temperatures for the $x = 0.10$, 0.0, and -0.10 samples are shown in Figs. 3(a)–3(c). The linear behavior seen for all the samples indicates single type of charge carriers. For the $x = -0.10$ and 0.0 samples, the positive R_{XY} values obtained indicate *p*-type conduction, while the negative values for the $x = 0.10$ sample are indicative of the *n*-type conduction. In Figs. 3(d) and 3(e), we display the absolute value of the Hall coefficient (R_H) and the charge carrier density (n) data for all the samples. The R_H and n roughly follow the $1/T$ behavior for $x = 0.0$, 0.05, and 0.10 with decreasing temperature, expected for semiconductors. For $x = -0.05$ and -0.10 , the R_H and n show complex temperature dependence and remain essentially unchanged between 300 and 10 K, similar to degenerate semiconductors.

Thus, our Hall data clearly demonstrate the transition from a *p*-type semiconductor to an *n*-type semiconductor for the CoSbS_{1+x} system achieved by increasing the sulfur excess used in the sample synthesis. Moreover, the charge carrier density shows a systematic increase for the nominally sulfur-rich samples, and it rises strongly for sulfur-deficient samples [Fig. 3(d)].

D. Thermoelectric transport properties

The temperature dependences of electrical resistivity, the Seebeck coefficient, and the power factor are presented in Fig. 4 for our sulfur-controlled CoSbS_{1+x} samples. The temperature dependence of heat capacity and mean free paths are presented in Fig. 5.

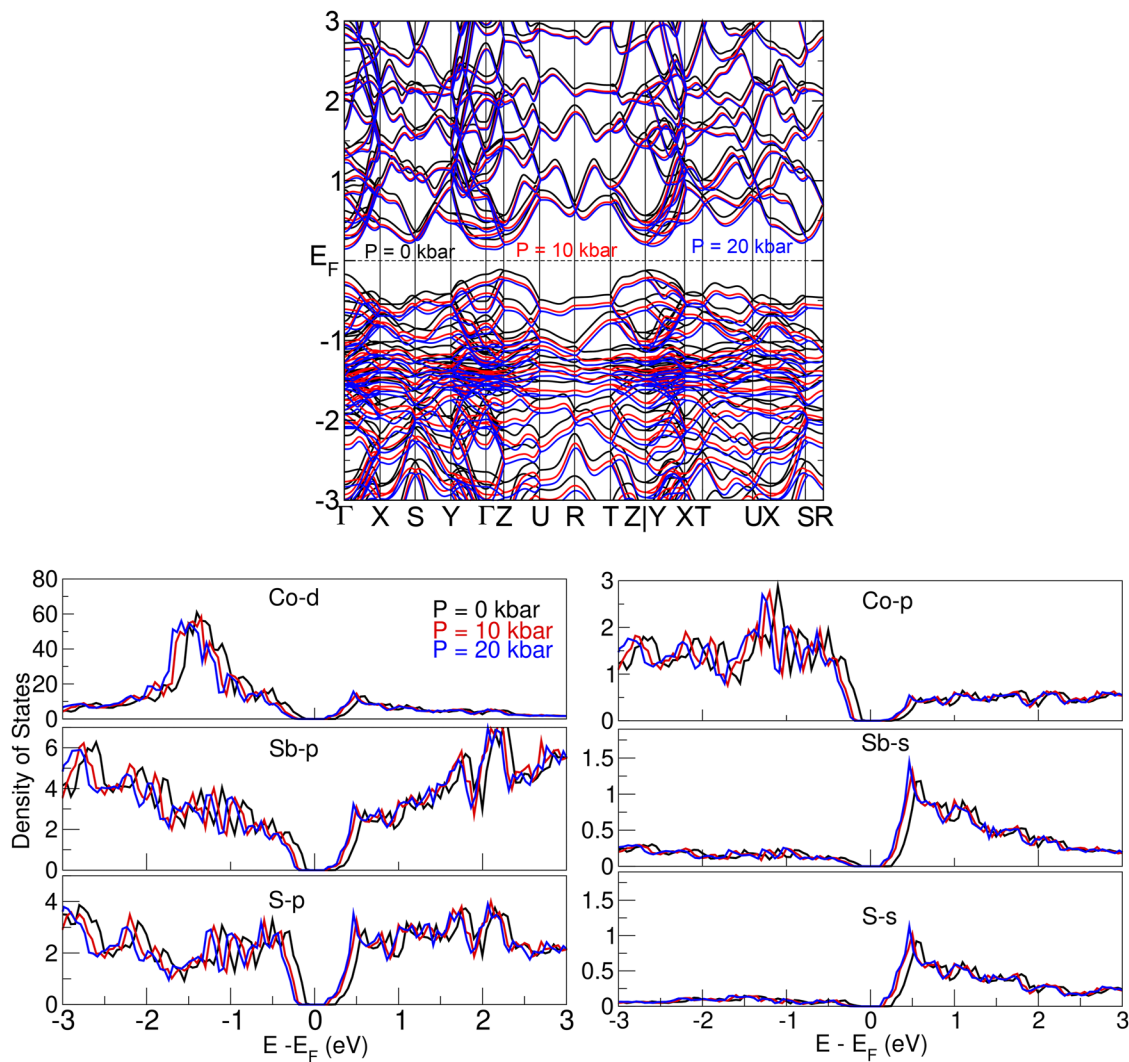


FIG. 2. Electronic band structure and partial density of states for uncompressed and compressed CoSbS.

1. Electrical resistivity

A typical semiconducting behavior can be seen for all the samples as electrical resistivity decreases with increasing temperature [Fig. 4(a)]. We have collected the 300-K ρ values of all the samples in Table I. The room-temperature ρ value for the $x = 0.0$ sample is $0.28 \Omega \text{ m}$ and rises exponentially to a large value of $1.53 \times 10^8 \Omega \text{ m}$ at 10 K. The sulfur-rich samples with $x = 0.05$ and 0.10 show significantly lower room-temperature ρ values, i.e., 0.0141 and $0.0036 \Omega \text{ m}$, respectively. At low temperatures, ρ increases exponentially to a value of 1.88×10^5 and $1.29 \times 10^5 \Omega \text{ m}$ for $x = 0.05$ and 0.10 , respectively. The suppressed resistivity of these samples compared to the $x = 0.0$ sample derives from the increased carrier concentration. Similarly, the sulfur-deficient samples of $x = -0.05$ and -0.1 show much lower ρ values than the $x = 0.0$ sample, apparently due to a doping effect. Upon cooling, ρ increases rapidly, up to 1.36×10^5

and $3.57 \Omega \text{ m}$ for $x = -0.05$ and -0.10 at 2 K. The bandgap energies were estimated by using the Arrhenius equation in the high temperature region by linear fitting of $\log(\rho)$ vs $1/T$ as shown in Fig. 4(b); these results are also summarized in Table I. Indeed, the bandgap is the largest for the $x = 0.0$ sample, and both increasing or decreasing the (nominal) sulfur content results in a reduction in the bandgap energy.

2. Seebeck coefficient

The most significant observation from the Seebeck coefficient vs the temperature data shown in Fig. 4(c) is that within the entire temperature range (50–300 K) measured, the Seebeck coefficient is positive for the (nominally) sulfur-deficient $x = 0.0$, -0.05 , and -0.10 samples indicative of *p*-type conduction, while the sulfur-rich $x = 0.05$ and 0.10 samples show *n*-type negative Seebeck coefficient values. The Seebeck coefficient at 300 K for all the samples is given

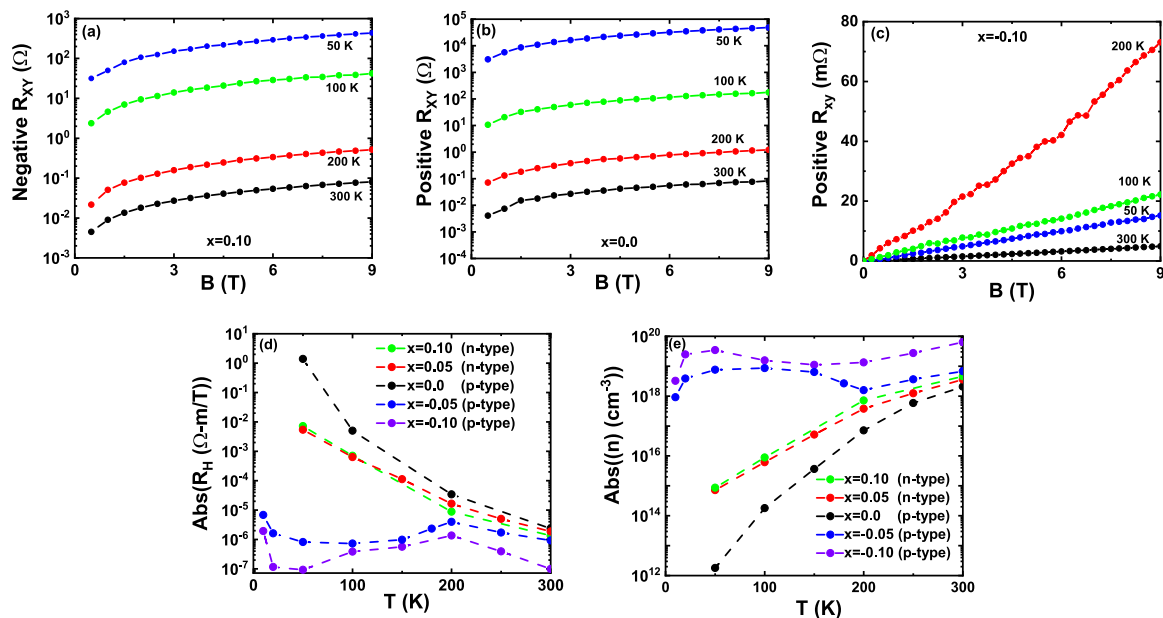


FIG. 3. The Hall measurement data for the CoSbS_{1+x} samples. The magnetic field dependence of the Hall resistance measured at different temperatures for (a) $x = 0.10$ with negative (*n*-type), and (b) $x = 0.0$ and (c) $x = -0.10$ with positive (*p*-type). The temperature dependence of (d) absolute value of the Hall coefficient and (e) charge carrier density for all samples.

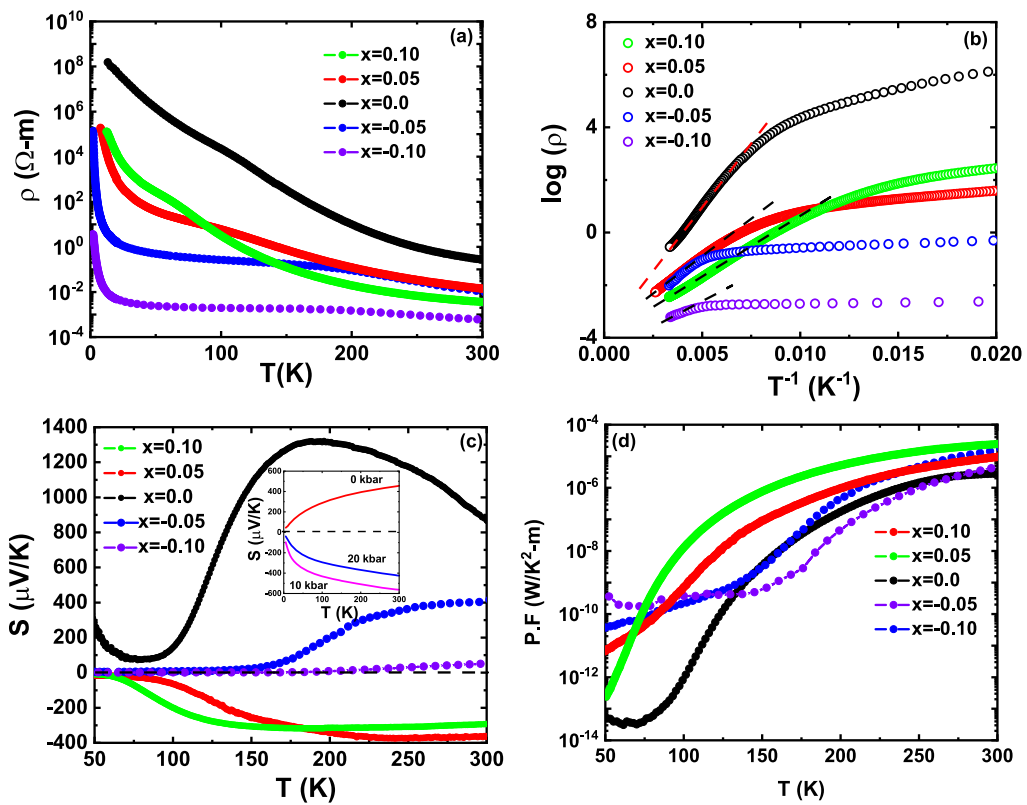


FIG. 4. Temperature-dependent thermoelectric properties for the CoSbS_{1+x} samples. (a) Electrical resistivity. (b) Arrhenius plots: $\log(\rho)$ vs $1/T$ (K^{-1}) with linear fit of the data in high temperature region of activated transport; symbols represent experimental data, and black and red dashed lines indicate linear fits of the data. (c) The Seebeck coefficient (inset: DFT calculated Seebeck coefficient by using experimental charge carrier density for CoSbS). (d) Power factor (PF).

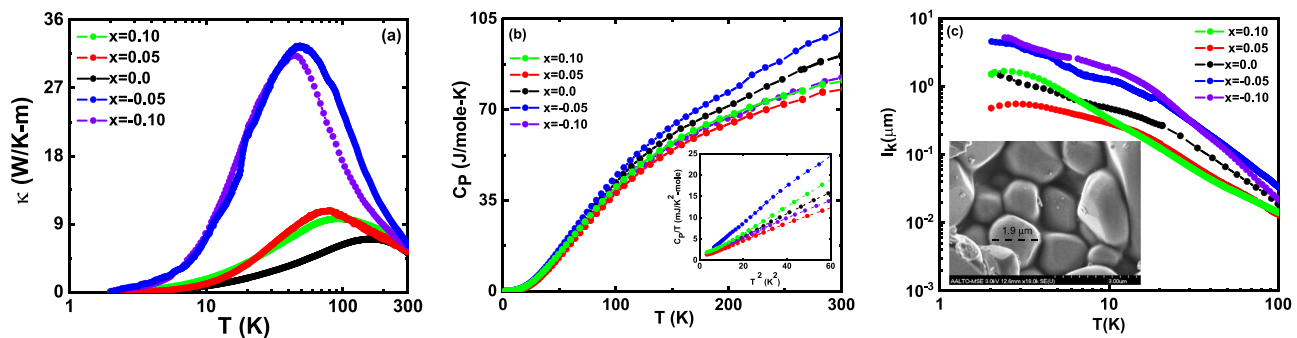


FIG. 5. (a) Thermal conductivity, (b) heat capacity, and (c) phonon mean free path vs temperature for the CoSbS_{1+x} samples. Inset of (b): Debye model fits in the low temperature range. Inset of (c): SEM image of the $x = 0.0$ sample showing the grain size of $1.9 \mu\text{m}$ found to be close to MFP $1.53 \mu\text{m}$ at 2 K.

TABLE I. Thermoelectric transport properties measured at 300 K for the CoSbS_{1+x} samples; the bandgap energies are calculated by using the Arrhenius equation by linear fitting of $\log(\rho)$ vs $1/T$ in the high temperature. The Debye temperature (θ_D), the Sommerfeld coefficient (γ), and the mean free path (MFP) (l_k) at 2 K.

Sample	Bandgap (eV)	ρ ($\Omega \text{ m}$)	S ($\mu\text{V}/\text{K}$)	κ (W/K m)	PF (W/m K ²)	ZT	θ_D (K)	γ (J/mol K ²)	l_k (μm) at 2 K
$x = -0.10$	0.032	6.032×10^{-4}	50	6.23	4.14×10^{-6}	1.99×10^{-4}	203.27	6.81×10^{-4}	5.22
$x = -0.05$	0.11	9.66×10^{-3}	403	6.02	1.68×10^{-5}	8.37×10^{-4}	166.41	3.95×10^{-4}	4.57
$x = 0.0$	0.15	0.28	879	5.2	2.75×10^{-6}	1.58×10^{-4}	192.47	1.53×10^{-4}	1.53
$x = 0.05$	0.109	0.0141	-362	5.65	9.29×10^{-6}	3.33×10^{-4}	217.1	7.488×10^{-4}	0.48
$x = 0.10$	0.038	0.0036	-294	6.25	2.4×10^{-5}	1.15×10^{-3}	184.28	3.81×10^{-4}	1.50

in Table I. In the inset of Fig. 4(c), we show the DFT calculated Seebeck coefficient values for CoSbS under compression (calculated by using the charge carrier density value from the 300-K Hall measurement); similarly, to the experimental data, the positive Seebeck coefficient of uncompressed CoSbS turns to negative upon pressure application. The Seebeck results are important because they reveal that we can synthesize both *p*-type and *n*-type samples from the same elemental precursors (Co, Sb, and S) by simply controlling the nominal excess or deficiency of the amount of sulfur used in the synthesis.

3. Power factor

The PF vs temperature dependence for all the samples is presented in Fig. 4(d). The PF at high temperature was increased for both *n*-type ($x = 0.10, 0.05$) and *p*-type ($x = -0.05, -0.1$) samples compared to the *p*-type $x = 0.0$ sample.

4. Thermal conductivity

The temperature dependent thermal conductivity measurement data are presented in Fig. 5(a), and the room-temperature κ values are given in Table I. At all temperatures, the thermal conductivity is the lowest for the $x = 0.0$ sample, and with both increasing or decreasing x , the κ values are found to increase. We believe this increase in $k_T = (\kappa_e + \kappa_l)$ is mostly due to an increased lattice thermal conductivity κ_l , as the electronic thermal conductivity κ_e value estimated by using the Wiedemann–Franz law ($\kappa e_e = L \sigma T$), where L is the Lorentz number ($2.44 \times 10^{-8} \text{ V}^2 \text{ K}^{-2}$), σ is the electrical conductivity, and T is the absolute temperature was found to be negligible for all samples. On cooling to lower temperatures, the value

of κ increases and reaches a maximum for all samples. The measured room temperature thermal conductivity values as well as the temperature dependence behavior seen are in line with the earlier reports for CoSbS .^{34,35,39} With increasing x , the peak in κ is strongly enhanced for the sulfur-deficient samples and moves to lower temperatures. The increase in peak κ value could be explained by the phonon mean free path (MFP).

5. Heat capacity and phonon mean free path

In Fig. 5(b), we show the heat capacity data for the samples; the inset of the figure illustrates the analysis of the low temperature data by using the Debye model: $C_p = \frac{12\pi^4}{5} R(T\theta_D)^3 + \gamma T$. The resultant Debye temperature (θ_D) and the Sommerfeld coefficient (γ) values are collected in Table I. The temperature dependence of the phonon MFP was then evaluated by using Fourier's law ($\kappa_l = \frac{1}{3} C \rho_d v l_k$) with the Debye model, where C , ρ_d , v , and l_k are the specific heat, density, phonon velocity, and MFP of the phonons involved in the thermal conductivity, respectively. The value of v was estimated from θ_D for each sample. From Fig. 5(c), the phonon MFP increases with decreasing temperature; the 2 K values are given in Table I. Interestingly, for the nominally sulfur-deficient $x < 0$ samples, the MFP values are the largest in line with their increased thermal conductivity. The experimental MFP value approaches the grain size at low temperature, as shown for the $x = 0.0$ sample in the inset of Fig. 5(c), indicating the dominance of phonon scattering from the grain boundaries.

The values of thermoelectric PF and ZT at 300 K are presented in Table I. The PF and ZT values of both *p*-type and *n*-type

compositions can be optimized by decreasing and increasing the nominal sulfur content used in sample synthesis. For the present samples, we were able to realize nine times and six times enhanced ZT values for the n -type ($x = 0.10$) and p -type ($x = -0.05$) samples, respectively, compared to the $x = 0.0$ sample. However, the measured PF and ZT values for our samples are still significantly low as compared to Te doped samples synthesized by using spark plasma sintering (SPS) by Guélou *et al.*⁵⁰

IV. CONCLUSIONS

We have demonstrated that the thermoelectric CoSbS_{1+x} material can be tailored for both p -type and n -type semiconductors (see Fig. 6) by simply controlling the sulfur vapor pressure during the solid-state material synthesis. The tiny sulfur excess ($0 < x \leq 0.1$) produces n -type semiconducting samples, while the sulfur-deficient ($-0.1 \leq x \leq 0$) condition yields p -type semiconducting samples. The types and densities of the carriers were systematically investigated by the Seebeck and the Hall effect measurements. Structurally, the p -type to n -type transition was reflected in the lattice parameters, which showed their maximum values around the p - n turning point. Computationally, the situation could be simulated through first principle DFT calculations by applying compressive pressure on CoSbS . The uncompressed CoSbS appeared as a p -type semiconductor with an indirect bandgap of 0.38 eV, while the pressure application turned CoSbS into an n -type semiconductor without significantly affecting the bandgap. The increased charge carrier density and strongly enhanced phonon mean free path resulted in strongly enhanced thermal conductivity for the sulfur-deficient $x < 0$ samples. We show that by controlling the excess sulfur used in the synthesis, we can achieve an increase of nine times and six times in power factor for n -type and p -type CoSbS_{1+x} materials, respectively. Our study underlines the importance of precise composition tuning in exploring and exploiting the multiple thermodynamic states in a single-phase CoSbS_{1+x} material. The possibility to realize both p -type and n -type semiconductivity in a single material system is a highly attractive feature for thermoelectric application.

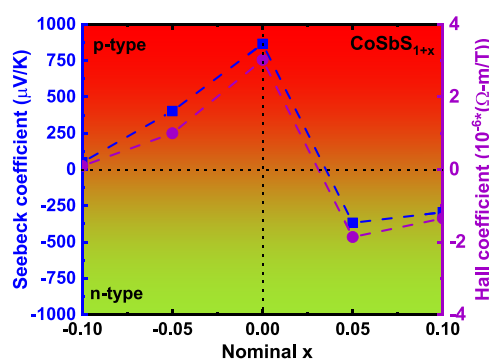


FIG. 6. The p -type to n -type conductivity transition with x in CoSbS_{1+x} . The transition is confirmed by both the Seebeck coefficient (left) and the Hall coefficient (right).

SUPPLEMENTARY MATERIAL

See the [supplementary material](#) for Fig. S1. Rietveld refined XRD patterns for CoSbS_{1+x} samples. Table SI. Summary of refined atomic positions. Table S2. Summary of refined lattice parameters. Table S3. Summary of theoretically calculated lattice parameters for compressed and uncompressed CoSbS .

ACKNOWLEDGMENTS

We acknowledge the funding from the Academy of Finland (Profi3 and PREIN). This work made use of the RawMatters Finland Infrastructure (RAMI) facilities at Aalto University.

AUTHOR DECLARATIONS

Conflict of Interest

The authors have no conflicts to disclose.

Author Contributions

H Sajida Kousar: Conceptualization (equal); Data curation (equal); Formal analysis (equal); Investigation (equal); Methodology (equal); Software (equal); Writing – original draft (equal); Writing – review & editing (equal). **Divya Srivastava:** Conceptualization (supporting); Data curation (supporting); Formal analysis (supporting); Investigation (supporting); Software (lead); Writing – review & editing (supporting). **Antti J Karttunen:** Visualization (equal); Writing – review & editing (supporting). **Maarit Karppinen:** Conceptualization (equal); Funding acquisition (equal); Supervision (equal); Validation (equal); Visualization (equal); Writing – original draft (equal); Writing – review & editing (equal). **Girish C Tewari:** Conceptualization (lead); Data curation (equal); Formal analysis (equal); Investigation (equal); Methodology (equal); Resources (equal); Supervision (equal); Validation (equal); Visualization (equal); Writing – original draft (equal); Writing – review & editing (equal).

DATA AVAILABILITY

The data that support the findings of this study are available from the corresponding authors upon reasonable request.

REFERENCES

- I. S. Khan, K. N. Heinselman, and A. Zakutayev, *J. Phys.: Energy* **2**, 032007 (2020).
- H. Morkoç, *Nitride Semiconductors and Devices*, 32nd ed. (Springer, Berlin, 1999).
- J.-S. Hu, L.-L. Ren, Y.-G. Guo, H.-P. Liang, A.-M. Cao, L.-J. Wan, and C.-L. Bai, *Angew. Chem., Int. Ed.* **44**, 1269 (2005).
- H. Tamaki, H. K. Sato, and T. Kanno, *Adv. Mater.* **28**, 10182 (2016).
- S. Ohno, K. Imasato, S. Anand, H. Tamaki, S. D. Kang, P. Gorai, H. K. Sato, E. S. Toberer, T. Kanno, and G. J. Snyder, *Joule* **2**, 141 (2018).
- F. Ren and J. C. Zolper, *Wide Energy Bandgap Electronic Devices* (World Scientific Publishing Co. Pte. Ltd., Singapore, 2003).
- G. Peleckis, T. Motohashi, M. Karppinen, and H. Yamauchi, *Appl. Phys. Lett.* **83**, 5416 (2003).
- P. Jood, G. Peleckis, X. L. Wang, S. X. Dou, H. Yamauchi, and M. Karppinen, *J. Appl. Phys.* **107**, 09D716 (2010).
- J. Piprek, *Opt. Quantum Electron.* **44**, 67 (2012).

- ¹⁰C. P. Wang and Y. R. Wu, *J. Appl. Phys.* **112**, 033104 (2012).
- ¹¹J. Li, N. Gao, D. Cai, W. Lin, K. Huang, S. Li, and J. Kang, *Light: Sci. Appl.* **10**, 129 (2021).
- ¹²Q. Gao, L. Fu, H. Chen, and M. Wan, *J. Appl. Phys.* **124**, 085708 (2018).
- ¹³G. Li, W. Wang, W. Yang, Y. Lin, H. Wang, Z. Lin, and S. Zhou, *Rep. Prog. Phys.* **79**, 056501 (2016).
- ¹⁴B. J. Baliga, *Semicond. Sci. Technol.* **28**, 074011 (2013).
- ¹⁵J. S. Blakemore, *J. Appl. Phys.* **53**, R123 (1982).
- ¹⁶S. B. Zhang and J. Northrup, *Phys. Rev. Lett.* **67**, 2339 (1991).
- ¹⁷Q. Guo, D. Berthebaud, J. Ueda, S. Tanabe, A. Miyoshi, K. Maeda, and T. Mori, *J. Mater. Chem. C* **7**, 8269 (2019).
- ¹⁸G. D. Mahan, *APL Mater.* **4**, 104806 (2016).
- ¹⁹Y. Qin, Y. Xiao, and L. D. Zhao, *APL Mater.* **8**, 010901 (2020).
- ²⁰G. C. Tewari, T. S. Tripathi, H. Yamauchi, and M. Karppinen, *Mater. Chem. Phys.* **145**, 156 (2014).
- ²¹T.-L. Chou, G. C. Tewari, T.-S. Chan, Y.-Y. Hsu, H. Yamauchi, and M. Karppinen, *Solid State Commun.* **206**, 12 (2015).
- ²²T.-L. Chou, G. C. Tewari, D. Srivastava, A. Yamamoto, T.-S. Chan, Y.-Y. Hsu, J.-M. Chen, H. Yamauchi, and M. Karppinen, *Mater. Chem. Phys.* **177**, 73 (2016).
- ²³T. L. Chou, G. C. Tewari, T. S. Chan, Y. Y. Hsu, J. M. Chen, H. Yamauchi, and M. Karppinen, *Eur. J. Inorg. Chem.* **2015**, 2574.
- ²⁴G. C. Tewari, T. S. Tripathi, and A. K. Rastogi, *J. Electron. Mater.* **39**, 1133 (2010).
- ²⁵C. F. Wu, T. R. Wei, and J. F. Li, *APL Mater.* **4**, 104801 (2016).
- ²⁶A. V. Powell, *J. Appl. Phys.* **126**, 100901 (2019).
- ²⁷J. F. Rowland, E. J. Gabe, and S. R. Hall, *Can. Mineral.* **13**, 188 (1975).
- ²⁸M. A. Zakrzewski, E. A. J. Burke, and H. W. Nugteren, *Can. Mineral.* **18**, 165 (1980).
- ²⁹L. J. Cabri, D. C. Harris, and J. M. Stewart, *Can. Mineral.* **10**(2), 232–246 (1970).
- ³⁰R. Henry, J. Steger, H. Nahigian, and A. Wold, *Inorg. Chem.* **14**, 2915 (1975).
- ³¹L. J. Cabri, D. C. Harris, and J. M. Stewart, *Am. Mineral.* **55**, 10 (1970).
- ³²H. Nahigian, J. Steger, H. L. McKinzie, R. J. Arnott, and A. Wold, *Inorg. Chem.* **13**, 1498 (1974).
- ³³R. Chmielowski, S. Bhattacharya, W. Xie, D. Péré, S. Jacob, R. Stern, K. Moriya, A. Weidenkaff, G. K. H. Madsen, and G. Dennler, *J. Mater. Chem. C* **4**, 3094 (2016).
- ³⁴R. Chmielowski, S. Bhattacharya, S. Jacob, D. Péré, A. Jacob, K. Moriya, B. Delatouche, P. Roussel, G. Madsen, and G. Dennler, *Sci. Rep.* **7**, 46630 (2017).
- ³⁵D. Parker, A. F. May, H. Wang, M. A. McGuire, B. C. Sales, and D. J. Singh, *Phys. Rev. B* **87**, 045205 (2013).
- ³⁶P. Kaur and C. Bera, *Phys. Chem. Chem. Phys.* **19**, 24928 (2017).
- ³⁷J. Yang, D. Yang, Y. Wang, X. Quan, and Y. Li, *J. Solid State Chem.* **302**, 122443 (2021).
- ³⁸Z. Liu, H. Geng, J. Shuai, Z. Wang, J. Mao, D. Wang, Q. Jie, W. Cai, J. Sui, and Z. Ren, *J. Mater. Chem. C* **3**, 10442 (2015).
- ³⁹H. S. Kousar, D. Srivastava, M. Karppinen, and G. C. Tewari, *J. Phys.: Condens. Matter* **31**, 405704 (2019).
- ⁴⁰Q. Du, M. Abeykoon, Y. Liu, G. Kotliar, and C. Petrovic, *Phys. Rev. Lett.* **123**, 076602 (2019).
- ⁴¹A. O. Moghaddam, A. Shokuhfar, and A. Cabot, *Iran J. Mater. Sci. Eng.* **16**, 20 (2019).
- ⁴²Y. You, X. Su, S. Hao, W. Liu, Y. Yan, T. Zhang, M. Zhang, C. Wolverton, M. G. Kanatzidis, and X. Tang, *J. Mater. Chem. A* **6**, 15123 (2018).
- ⁴³Y. You, X. Su, W. Liu, Y. Yan, J. Fu, X. Cheng, C. Zhang, and X. Tang, *J. Solid State Chem.* **262**, 1 (2018).
- ⁴⁴Y. You, X. Su, W. Liu, Y. Yan, T. Hu, C. Uher, and X. Tang, *RSC Adv.* **7**, 34466 (2017).
- ⁴⁵P. Giannozzi, O. Andreussi, T. Brumme, O. Bunau, M. Buongiorno Nardelli, M. Calandra, R. Car, C. Cavazzoni, D. Ceresoli, M. Cococcioni, N. Colonna, I. Carnimeo, A. Dal Corso, S. De Gironcoli, P. Delugas, R. A. Distasio, A. Ferretti, A. Floris, G. Fratesi, G. Fugallo, R. Gebauer, U. Gerstmann, F. Giustino, T. Gorni, J. Jia, M. Kawamura, H.-Y. Ko, A. Kokalj, E. Küçükbenli, M. Lazzeri, M. Marsili, N. Marzari, F. Mauri, N. L. Nguyen, H.-V. Nguyen, A. Otero-De-La-Roza, L. Paulatto, S. Poncé, D. Rocca, R. Sabatini, B. Santra, M. Schlipf, A. P. Seitsonen, A. Smogunov, I. Timrov, T. Thonhauser, P. Umari, N. Vast, X. Wu, and S. Baroni, *J. Phys.: Condens. Matter* **29**, 465901 (2017).
- ⁴⁶P. Giannozzi, S. Baroni, N. Bonini, M. Calandra, R. Car, C. Cavazzoni, D. Ceresoli, G. L. Chiarotti, M. Cococcioni, I. Dabo, A. Dal Corso, S. de Gironcoli, S. Fabris, G. Fratesi, R. Gebauer, U. Gerstmann, C. Gougoussis, A. Kokalj, M. Lazzeri, L. Martin-Samos, N. Marzari, F. Mauri, R. Mazzarello, S. Paolini, A. Pasquarello, L. Paulatto, C. Sbraccia, S. Scandolo, G. Scaluzero, A. P. Seitsonen, A. Smogunov, P. Umari, and R. M. Wentzcovitch, *J. Phys.: Condens. Matter* **21**, 395502 (2009).
- ⁴⁷J. P. Perdew, K. Burke, and M. Ernzerhof, *Phys. Rev. Lett.* **77**, 3865 (1996).
- ⁴⁸K. F. Garrity, J. W. Bennett, K. M. Rabe, and D. Vanderbilt, “Pseudopotentials for high-throughput DFT calculations,” *Comput. Mater. Sci.* **81**, 446–452 (2014).
- ⁴⁹G. K. H. Madsen, J. Carrete, and M. J. Verstraete, *Comput. Phys. Commun.* **231**, 140 (2018).
- ⁵⁰G. Guélou, F. Failamani, P. Sauerschnig, J. Waybright, K. Suzuta, and T. Mori, *J. Mater. Chem. C* **8**, 1811 (2020).